IEEE Access
Multidisciplinary | Rapid Review | Open Access Journal

Received March 10, 2020, accepted March 26, 2020, date of publication April 6, 2020, date of current version April 17, 2020.

Digital Object Identifier 10.1109/ACCESS.2020.2985858

Wide-Field 3D Ultrasound Imaging Platform With a Semi-Automatic 3D Segmentation Algorithm for Quantitative Analysis of Rotator Cuff Tears

MOON HWAN LEE[1], JUN-YOUNG KIM[2], KYUNGSU LEE[1], CHANG-HYUK CHOI[2], AND JAE YOUN HWANG[1], (Member, IEEE)

[1]Department of Information and Communication Engineering, Daegu Gyeongbuk Institute of Science and Technology, Daegu 42988, South Korea
[2]Department of Orthopedic Surgery, Daegu Catholic University Medical Center, Daegu 42472, South Korea

Corresponding authors: Chang-Hyuk Choi (chchoi@cu.ac.kr) and Jae Youn Hwang (jyhwang@dgist.ac.kr)

This work was supported by the Ministry of Trade, Industry and Energy (MOTIE) of the Republic of Korea under Grant 10085624.

ABSTRACT Rotator cuff tear (RCT) is a common injury that causes pain and disability in adults. The quantitative diagnosis of the RCT can be crucial in determining a treatment plan or monitoring treatment efficacy. Currently, only a few diagnosis tools, such as magnetic resonance imaging (MRI) and ultrasound imaging (US), are utilized for the diagnosis. Specifically, US exhibited comparable performance with MRI while offering a readily available diagnosis of RCTs at a lower cost. However, three-dimensional(3D) US and analysis of the regions are necessary to enable a better diagnosis of RCTs. Therefore, we developed a wide-field 3D US platform with a semi-automatic 3D image segmentation algorithm for 3D quantitative diagnosis of RCTs. The 3D US platform is built based on a conventional 2D US system and obtains 3D US images via linear scanning. With respect to 3D segmentation algorithm based on active contour model, frequency compounding and anisotropic diffusion methods were applied, and their effects on segmentation were discussed. The platform was used for clinical examination after evaluating the platform via the RCT-mimicking phantoms. As verified by the Dice coefficient(average DC: 0.663, volume DC: 0.723), which was approximately up to 50% higher than that obtained with conventional algorithms, the RCT regions segmented by the developed algorithm significantly matched the ground truth. The results indicated that the wide-field 3D US platform with the 3D segmentation algorithm can constitute a useful tool for improving the accuracy in the diagnosis of RCTs, and can eventually lead to better determination of treatment plans and surgical planning.

INDEX TERMS 3D ultrasound, rotator cuff tear, 3D image segmentation, active contour.

I. INTRODUCTION

Rotator cuff tear (RCT) is a common disease in the shoulder joint, which causes pain and a limited range of motion resulting in functional disability. The prevalence and severity of RCTs are expected to increase with elderly individuals [1]. The aging population is currently growing globally, and the number of patients with RCTs are also increasing. Nonsurgical or surgical treatment (open or arthroscopic repair) is performed to treat the RCT, and the estimation of the tear configuration is essential to determine the treatment method [2].

Non-invasive imaging techniques, such as ultrasound sonography (US) and Magnetic Resonance Imaging (MRI), increase the diagnostic accuracy of RCT due to a variety of technological advances [3]. Subsequently, MRI is considered as the favored imaging tool for diagnosis and surgical planning. However, this imaging modality is not clinically readily available due to its high cost, time consumption, and acoustic noise [4]. Conversely, US is widely used for diagnosis and surgical planning for RCTs due to its real-time dynamic capture, low-cost, time-saving, and readily-availability when compared to MRI [5]–[7]. Hence, US is more preferred than MRI by the patients [8]. Furthermore, Roy *et al.* [9] reported that US exhibits high sensitivity and specificity for the diagnosis of RCT, and several studies described that US exhibited

The associate editor coordinating the review of this manuscript and approving it for publication was Gustavo Callico.

a similar or better diagnostic performance when compared to that of MRI [10]–[13].

However, a conventional US is a tool in which the two-dimensional (2D) images are acquired by an operator; therefore, the diagnosis is determined based on the skill and subjectivity of the surgeon. Hence, the three-dimensional (3D) shape cannot be accurately understood. To overcome the aforementioned disadvantages, 3D US is introduced [14], [15]. Free-hand scanning, 2D matrix array transducer, and mechanical scanning are representative techniques for 3D US with their pros and cons [14], [16]. Specifically, 3D US techniques are used and researched for various applications and the diagnosis of RCTs [17]–[21].

Among the techniques, the 2D matrix array transducer was recently commercialized and is relatively widely used for clinical purposes such as monitoring fetuses. However, the conventional 3D US(2D matrix array) exhibits a small field of view (GE RSP6-16, 37.4 mm X 29° FoV) and is unable to trace the convexity of shoulder surface during free-hand scanning, and this can constitute an obstacle to accurately diagnose RCTs and determine the severity of the RCT [22]. Additionally, it is not clinically utilized widely due to the high cost ($3500). Free-hand scanning with the capability of providing a wide field of view with a position sensor appears as ideal for the application. However, the technique is unable to ensure the reliability of the 3D imaging and even requires calibration [15], [23], which can act as a barrier for use in clinics. Additionally, the reconstruction of a 3D image with the 2D matrix array and free-hand scanning is extremely complex such that it needs unique algorithms with high computational cost and takes a considerably long time to reconstruct [14]. Conversely, mechanical scanning can offer 3D imaging with a comparatively simple configuration and algorithm [15]. Even if the technique requires a scanning apparatus to move the probe over the region of interest, it can be implemented at a relatively low cost [15].

Although the 2D matrix array and free-hand scanning were utilized for the diagnosis of RCT [24], [25], their use is limited to only research purposes and cannot be used further due to the high cost of the hardware and difficulty in configuration. Therefore, a 3D US system for clinical use, which is capable of offering a large field of view for a 3D US image with a reasonable cost, should be developed for the quantitative analysis of the RCT region. Hence, we utilized mechanical scanning, particularly linear scanning, in which scan conversion is simpler and credible due to the perpendicular scanning route to the image plane with the accurate information on the position of the transducer.

In addition to the 3D US system with a large field of view, 3D quantitative analysis of RCT regions and especially 3D volumetric segmentation is crucial to precisely estimate the tear configuration and decide surgical planning. Ultrasonic image segmentation enables delineating the boundary of an RCT on an ultrasound image. Recently, various methods including threshold, region growing, watershed, and active contour techniques were developed for ultrasound image segmentation. The threshold-based technique was successfully applied to the automatic segmentation of breast lesions on ultrasound images [26]. However, the technique exhibited poor performance in the segmentation of the diseased regions when imaging parameters, such as the dynamic range, focus, and gain, were changed.

Conversely, region growing and watershed-based techniques exhibited better performance than the threshold-based techniques in the segmentation of tumors and cysts on ultrasound images [27], [28]. However, the region growing and watershed-based segmentation methods were sensitive to noise. Therefore, their performance was dependent on the image quality. To overcome the issues, active contour-based models were developed to segment breast tumors in three-dimensional ultrasound images [19]. The active contour-based models were shown as superior to the region growing and threshold-based methods in the segmentation of breast tumor regions. Thus, an active contour model is generally utilized for US image segmentation [29]. Additionally, 3D US images were also adequately segmented with the extension of active contour model(2D segmentation algorithm) [30]–[32]. Therefore, we developed a semi-automatic 3D segmentation algorithm based on active contour model.

In the study, we developed and demonstrated a wide-field 3D US platform with a semi-automatic 3D segmentation algorithm for the quantitative detection of RCTs. The 3D US platform can adapt to the conventional 2D US system with relatively low cost for configuration. With the linear scanning apparatus, the 3D US platform exhibits a wide field of view, multi-planar image, and high repeatability for diagnosis at a specific region. Furthermore, the semi-automatic 3D ultrasound segmentation algorithm was developed based on active contour and some pre-processing methods. Specifically, frequency compounding and anisotropic diffusion were applied as pre-processing methods to suppress speckle noise and enhance contrast. Their effects on the segmentation were discussed, and an optimal suitable pre-processing procedure was selected. For better segmentation accuracy, we also approached the 3D segmentation algorithm based on active contour via exploiting randomly generated masks. Using the platform that integrates with the algorithm, phantom experiments and clinical tests were performed to evaluate it. Finally, comparisons were performed with the outcomes obtained from previous algorithms.

II. MATERIAL AND METHODS

A. 3D ULTRASOUND IMAGING SYSTEM

A 3D ultrasound imaging platform was developed for 3D ultrasound imaging of RCT regions in the shoulder with a large field of view. Figures 1.(a) and (b) show the 3D ultrasound imaging platform. The platform consists of a commercial linear array ultrasound imaging system (Sonix Touch Q+, BK Ultrasound, Canada), shoulder scanning apparatus, DAQ board (USB6341, National Instrument, USA), and user-interface program for the system control.

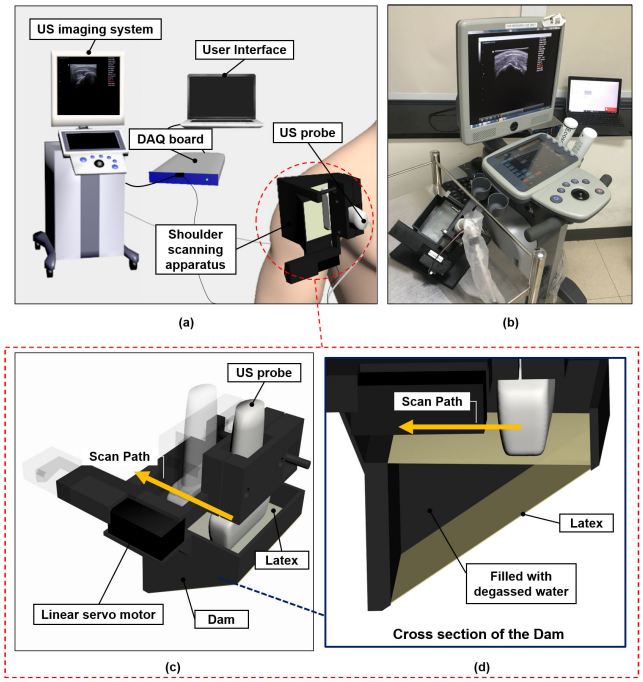

FIGURE 1. 3D ultrasound imaging platform for detection of rotator cuff tear regions.

The linear array ultrasound imaging system includes a 1D linear array probe (L14-5/38 Linear Transducer, BK Ultrasound, Canada), which includes 128-channel elements with a pitch size of 0.3 mm and an aperture size of 4 mm x 38 mm in the elevation and azimuth direction.

The shoulder scanning apparatus is shown in Fig. 1.(c). It consists of a degassed-water dam, a linear servo motor (L12-30PT-6, IRrobot, Republic of Korea), and an ultrasound probe. The shoulders are curved and rigid, and thus an air gap between the skin and ultrasound probe is formed when the probe is attached to the shoulder. It is noted that the ultrasound can be barely transmitted into the body from the air due to the high acoustic impedance difference between the air and body. Eventually, the air gap can deteriorate whole image quality and hinder proper diagnosis. Therefore, a degassed-water dam was constructed to remove the air gap. The dam was designed to flexibly fit the shape of the shoulder. The frame of the dam was printed using a 3D printer (u Print SE Plus, Stratasys, USA). A thin latex sheet was attached at the bottom and top of the frame, as shown in Fig. 1.(d), such that the dam can be flexibly deformed and thereby tightly attached to the shoulder. Degassed water filled up the dam, as shown in Fig. 1.(d), to adequately transmit the ultrasound with the removal of the air gap. The material that filled the dam was selected to maximize the transmissivity of ultrasound waves from the probe to the shoulder [33].

The linear servo motor enables the ultrasound probe to scan an area, and this is integrated with the shoulder scanning apparatus over the shoulder. The maximum travel range is less than 56 mm. The commercial linear array ultrasound imaging system is synchronized with the shoulder scanning apparatus via the DAQ board. After 3D ultrasound imaging is initiated, the pulse signal from a digital output port of the DAQ board is transmitted to the linear motor after obtaining a B-mode image at an initial position. The linear motor integrated with the ultrasound probe moves to the next target position with a step size of 1 mm. Subsequently, a B-mode image is obtained at the position, and this is followed by a recording of a frame-trigger counting value in the user-interface program to annotate the order of the B-mode images. The procedure is repeated until the motor reaches the end position of the apparatus. During the process, the positions of the probe (where the B-mode images are obtained) are also recorded with the corresponding B-mode images in order. The B-mode images are then orderly enumerated by recorded position information and reconstructed to a 3D ultrasound image. The 3D ultrasound image exhibits a field of view of 38 mm×90 mm×56 mm as a maximum and it takes approximately 10 s for a single scan to acquire the 3D image. It is noted that the field of view can be appropriately adjusted based on the imaging object.

B. 3D SEGMENTATION ALGORITHM FOR ROTATOR CUFF TEAR REGIONS

For the precise 3D segmentation of rotator cuff tear regions on a 3D ultrasound image, we developed a semi-automatic segmentation algorithm based on frequency compounding (FC), speckle reducing anisotropic diffusion(SRAD), and Chan-Vese active contour techniques. For US imaging modality, speckle noise and low contrast are inevitable, and this can lead to low accuracy segmentation. To reduce speckle noise and improve low contrast while preserving edges, we applied FC and SRAD in the frequency domain of the radio frequency (RF) beamformed signals and spatial domain of the US images, respectively. Adaptive histogram equalization (AHE) was also applied for further contrast enhancement.

With respect to the active contour, a mask should be initialized and the location of the mask is extremely important because it affects the performance of the algorithm. The automatic initialization of the masks is significantly more crucial for an extension of Chan–Vese active contour to segment the RCT region in 3D. Previous studies utilized the centroid (center of mass) of the previous segmented frame as an initial mask for a subsequent frame as an approach for automatic initialization of the masks. The previous approach exhibited excellent performance in the studies [30]–[32]. However, it exhibited a weakness in our task. Given the vague boundaries and irregular shape s of the RCT regions, the initial mask was often located on the out-of-bounds region and not region of interest(the RCT region). After a single wrong initialization, segmentation on the rest of the frames in the 3D image failed.

Therefore, a new approach (which seeds the masks randomly) was attempted to improve the previous approach. Hence, the previous approach using the centroid is essentially utilized, and it improves with the proposed approach. In the proposed approach, numerous masks are generated on the

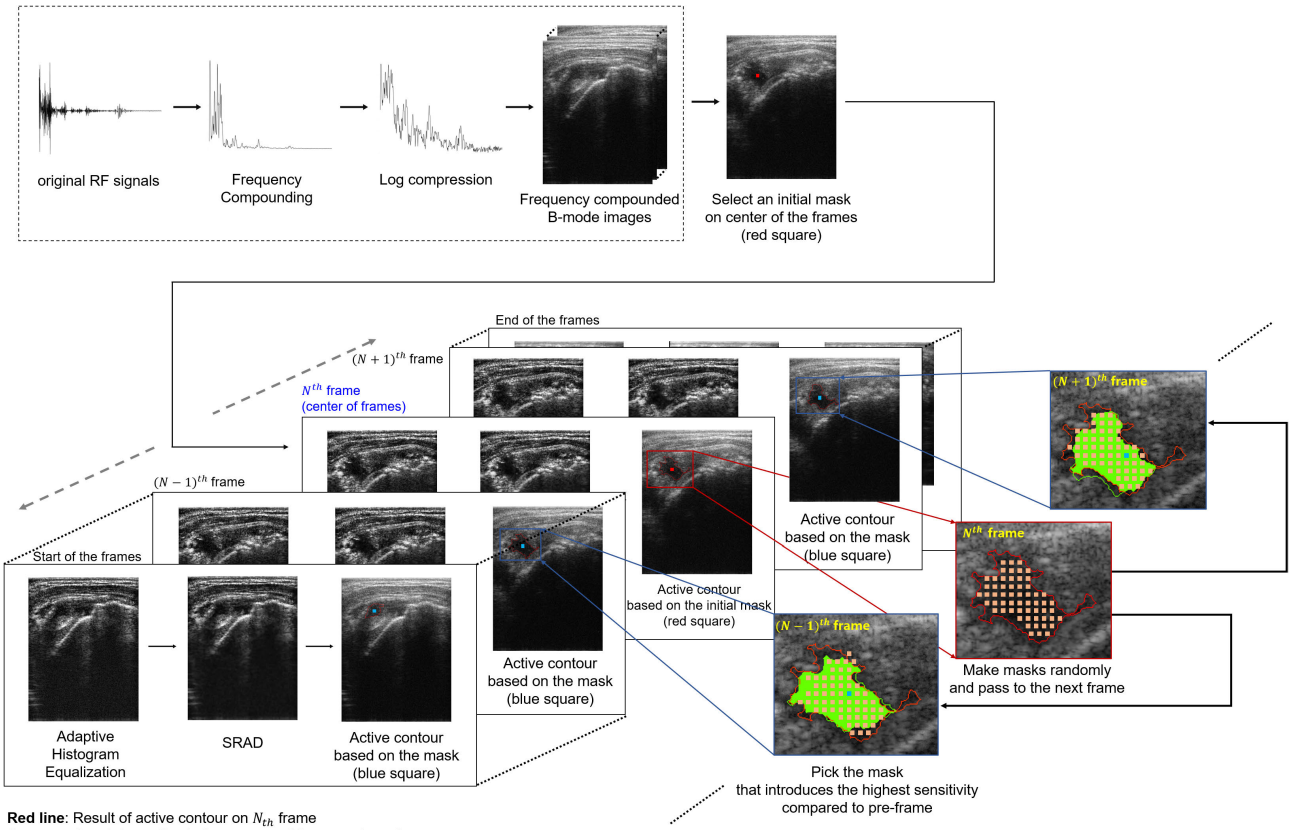

FIGURE 2. **Procedures for the 3D segmentation of rotator cuff tear regions on a 3D ultrasound image.**

frame based on the previous segmented frame when the mask on a subsequent frame is assumed as incorrectly initialized by using the centroid. The incorrectly initialized mask is determined by comparing the segmented result using the mask and previous segmented result. Chan-Vese active contour is then performed on all the masks with small iterations(to save time). If the masks were in the out-of-bound region, contoured results can be obtained as significantly different from the previous segmented frame. Conversely, if the masks were in the region of interest, contoured results can be similar to or at least laid over by the previous result. Thus, the contoured results of all the randomly generated masks were compared to the previously segmented result by the sensitivity metric. The mask with the highest sensitivity is then initialized as a mask of the frame, and the segmentation of images is performed with the mask.

The procedure is described in detail as follows: 1) Frequency compounding of beamformed RF signals; 2) Process for generating B-mode images; 3) Selection of an image located at the mid-frame among the series of 2D images, which contain the rotator cuff tear region; 4) Manual selection of an initial mask on the image by a doctor; 5) Image contrast enhancement by adaptive histogram equalization; 6) Application of SRAD to the enhanced image; 7) Perform the Chan-Vese active contour on the initial mask for the segmentation of the rotator cuff tear region; 8) Computation of the centroid of the segmented result and using the centroid in the subsequent frame; 9) Move on to the subsequent frame and repeat 5th and 6th step; 10) Perform active contour on the centroid with small iteration; 11) Compare the contoured result with the previous result; 12-1) Perform active contour with sufficient iterations if the centroid is assumed as proper mask for the frame; 12-2) Make numerous initial masks randomly on the frame based on the previous result if the centroid is assumed as wrongly located; 13) Perform the active contour on all the randomly generated masks with small iterations; 14) As an initial mask of the frame, select the optimal mask that results in segmentation with higher sensitivity when compared with the previous segmented frame; 15) Perform the active contour on the initial mask with sufficient iterations, and 16) Repeat the aforementioned steps from 8th step to 12th step and continue for all 2D images (Fig. 2).

All of the aforementioned steps including FC, SRAD, Chan-Vese active contour, and the 3D reconstruction algorithm were implemented using MATLAB and performed using a 3.4-GHz Intel Core i7 6700 CPU and 16-GB RAM.

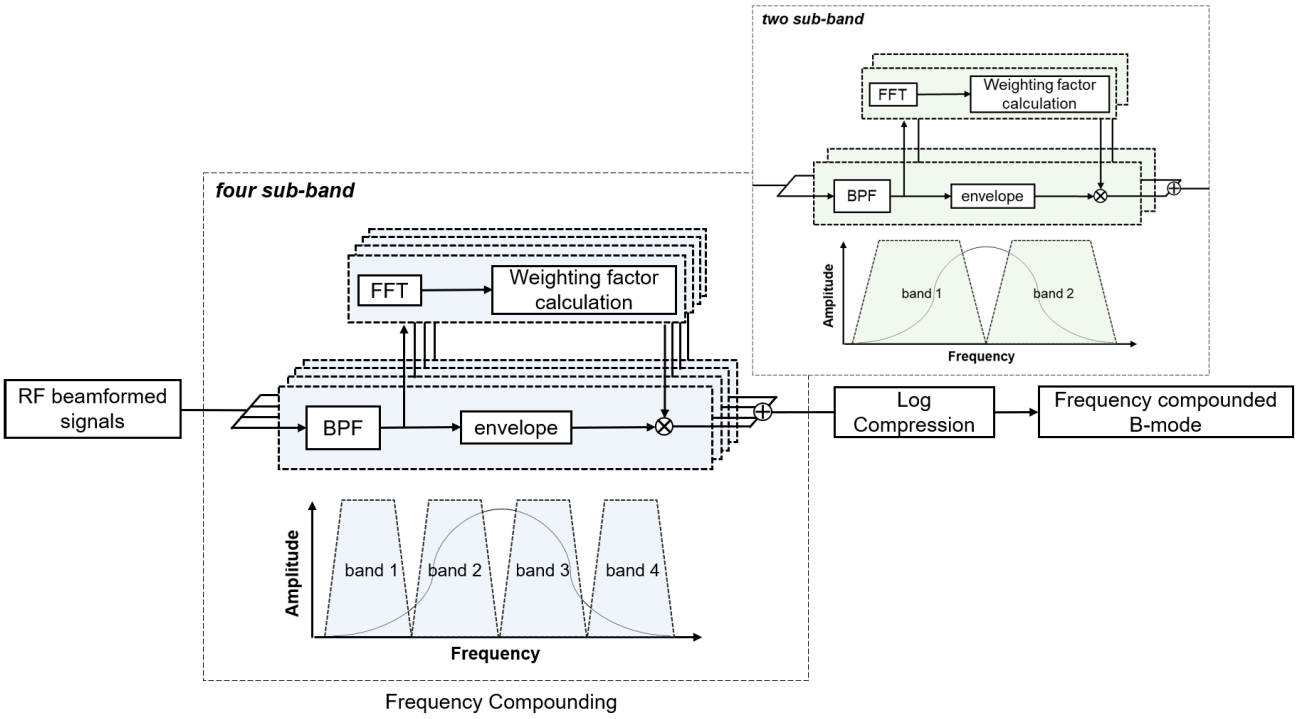

FIGURE 3. Frequency compounding of an ultrasound image.

1) FREQUENCY COMPOUNDING OF AN ULTRASOUND IMAGE

Frequency compounding techniques (which are also called frequency diversity [34]) were applied to construct a B-mode ultrasound image to suppress speckle noise and to improve the signal-to-noise ratio (SNR) of an ultrasound image. To divide the bandwidth of the A-line RF signals into sub-frequency bands, band-pass filters with different center frequencies, but with the same bandwidth, are applied to the RF signals. The signals within the divided bands are utilized to form sub-band images. A frequency compounding image is constructed via the weighted averaging of the sub-band images (Fig. 3). The weighting factors equalize the contribution of each sub-band and average the speckle patterns [35]. To determine the weighting factors for the construction of the frequency compounding image, integrated magnitudes of the sub-band signals are obtained with (1),

$$P_m = \sum_{k=0}^{N-1} |X_m(k)| \ , \tag{1}$$

where P_m denotes the integrated magnitude of the m^{th} sub-band signal; N denotes the number of utilized sub-bands. X_m denotes the m^{th} sub-band signal at the frequency domain, and k denotes the k_{th} frequency. With the integrated magnitudes of the sub-band signals, the weight factors for each sub-band are estimated with (2),

$$\omega_m = \frac{\prod_{k=0}^{M-1} P_k}{\sum_{i=0}^{M-1} \left[\prod_{j=0}^{M-1} P_j\right]_i} \ (k \neq m, \ j \neq i), \tag{2}$$

where ω_m denotes a weighting factor for the m_{th} sub-band image, and Π denotes the product of the sequences, and M is the number of sub-bands. Specifically for the denominator, all sub-bands are multiplied except for i_{th} sub-band. Hence, the products are obtained while varying the number i from 0 to $M-1$, following which they are summed.

2) SPECKLE REDUCING ANISOTROPIC DIFFUSION

To further reduce speckle noise in the frequency compounding image, an anisotropic diffusion technique with high edge-sensitivity was applied to the image. The anisotropic diffusion maintains edge contours in an ultrasound image while it decreases speckles. Therefore, the speckle reducing anisotropic diffusion method(SRAD), as suggested by Yu. et al [36], was utilized to reduce speckles on ultrasound images for the 3D segmentation of rotator cuff tear regions. In the anisotropic diffusion of the images, an instantaneous coefficient of variations at a local position is applied to a partial differential equation (PDE). The procedures are described in detail as follows: When an intensity image with a finite power and no zero values over an image supporting Ω is given, the output image is updated based on anisotropic diffusion partial difference equations (AD-PDE) as described in (3) and (4),

$$\frac{\partial I(x, y; t)}{\partial t} = div\left[c(q) \nabla I(x, y; t)\right] \tag{3}$$

$$I(x, \ y; 0) = I_0(x, \ y),$$

$$\frac{\partial I(x, y; t)}{\partial \vec{n}}|_{\partial\Omega} = 0, \tag{4}$$

where ∇ denotes the gradient operator; *div* denotes the divergence operator; $c(q)$ denotes the diffusion coefficient; q denotes the instantaneous coefficient of variations; I_0 denotes the initial image; $\partial\Omega$ denotes the border of Ω, and $\vec{n}$ denotes the outer normal to the $\partial\Omega$. The differential equation can be solved by an iterative Jacobi method. We assume the discrete image as $I^n_{i,\ j}$ (5) and solve the aforementioned PDE. It is noted that the time step-size of Δt and spatial step-size of h are sufficiently small:

$$\begin{aligned} &I^n_{i,\ j} = I(x,\ y,\ n\Delta t),\\ &(x = ih, y = jh, i = 0,\ 1,\ 2,\ \ldots M-1\\ &\&\ j = 0,\ 1,\ 2, \ldots\ N-1) \end{aligned} \tag{5}$$

where, $I^n_{i,\ j}$ denotes the image intensity at x, y, and $n\Delta t$; n denotes the time index; i is the i^{th} position in the x-direction; j denotes the j^{th} position in the y-direction; M denotes the pixel size of the image support in the x-direction, and N denotes the pixel size of the image support in the y-direction. The derivative and Laplacian approximation can be solved with symmetric boundary conditions. The derivative approximations is calculated with (6) and (7).

$$\nabla_R I^n_{i,j} = \left[\frac{I^n_{i+1,j} - I^n_{i,j}}{h}, \frac{I^n_{i,j+1} - I^n_{i,j}}{h}\right] \tag{6}$$

$$\nabla_L I^n_{i,j} = \left[\frac{I^n_{i,j} - I^n_{i-1,j}}{h}, \frac{I^n_{i,j} - I^n_{i,j-1}}{h}\right] \tag{7}$$

The Laplacian approximations is obtained with (8)

$$\nabla^2 I^n_{i,j} = \frac{I^n_{i+1,j} + I^n_{i-1,j} + I^n_{i,j+1} + I^n_{i,j-1} - 4I^n_{i,j}}{h^2} \tag{8}$$

The symmetric boundary conditions are illustrated with (9) and (10).

$$I^n_{M,j} = I^n_{M-1,j} j = 0,\ 1,\ 2, \ldots\ N-1 \tag{9}$$

$$I^n_{i,N} = I^n_{i,N-1} i = 0,\ 1,\ 2, \ldots\ M-1 \tag{10}$$

After the derivative and Laplacian approximations, the diffusion coefficient $c(q)$ is calculated with the following (11)-(14).

$$c^n_{i,j} = c[q(\frac{1}{I^n_{i,j}}\sqrt{\left|\nabla_R I^n_{i,j}\right|^2 + \left|\nabla_L I^n_{i,j}\right|^2},\ \frac{1}{I^n_{i,j}}\nabla^2 I^n_{i,j})] \tag{11}$$

$$c\,(q) = \frac{1}{1 + \left[q^2\,(x, y; t) - q_0^2\,(t)\right] / \left[q_0^2(t)(1 + q_0^2\,(t))\right]} \tag{12}$$

$$q(x, y; t) = \sqrt{\frac{\frac{1}{2}\left(\frac{|\nabla I|}{I}\right)^2 - \frac{1}{4^2}\left(\frac{\nabla^2 I}{I}\right)^2}{\left[1 + \frac{1}{4}\left(\frac{\nabla^2 I}{I}\right)\right]^2}} \tag{13}$$

$$q_0\,(t) = \frac{\sqrt{var\,[z\,(t)]}}{\overline{z(t)}} \tag{14}$$

where, $var\,[z\,(t)]$ denotes the intensity variance, and $\overline{z(t)}$ denotes the mean intensity over a homogeneous area at t.

After obtaining the diffusion coefficient $c(q)$, the divergence of $c(\cdot)\nabla I$ is calculated with symmetric boundary conditions for the AD-PDE with (15).

$$\begin{aligned} d^n_{i,j} = \frac{1}{h^2}\Big[&c^n_{i+1,j}\left(I^n_{i+1,j} - I^n_{i,j}\right) + c^n_{i,j}\left(I^n_{i-1,j} - I^n_{i,j}\right)\\ &+ c^n_{i,j+1}\left(I^n_{i,j+1} - I^n_{i,j}\right) + c^n_{i,j}\left(I^n_{i,j-1} - I^n_{i,j}\right)\Big] \end{aligned} \tag{15}$$

Finally, the approximation to the PDE is obtained by the anisotropic diffusion update function with (16). The approximation can result in a US image in which speckle noise is reduced, as shown in Fig. 4(b). The original image is shown in Fig. 4(a)

$$I^{n+1}_{i,j} = I^n_{i,j} + \frac{\Delta t}{4} d^n_{i,j} \tag{16}$$

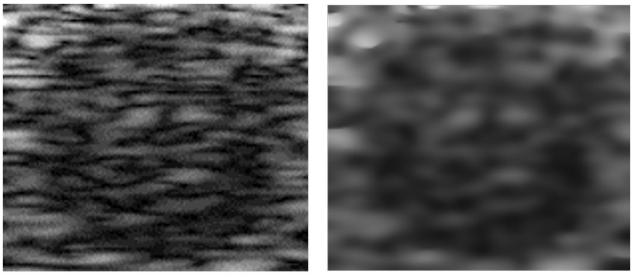

(a) (b)

FIGURE 4. Application of SRAD to US image of cyst phantom; (a) original (b) after SRAD.

3) CHAN-VESE ACTIVE CONTOUR ALGORITHM FOR SEGMENTATION OF ROTATOR CUFF TEAR REGIONS

To determine the boundary of rotator cuff tear regions on an ultrasound image, the active contour algorithm proposed by Chan and Vese [37] is applied to the anisotropic diffusion-filtered image. Before the algorithm is applied, an initial contour is manually selected on the filtered image. The Chan-Vese active contour algorithm is based on the Mumford–Shah function. This constitutes a powerful and flexible method that can segment various types of medical images, which cannot be properly segmented via classical segmentation methods such as thresholding or gradient-based methods. The algorithm is based on fitting an energy minimization problem such that it can be reformulated in the level set function. The segmentation boundary is represented implicitly with the level set function, which enables the segmentation to handle topological changes more easily than explicit snake methods. The algorithm computes forces generated from the attributes of an image. A contour is deformed by the forces. To determine a precise boundary of the regions of interest, the contour is deformed by the following procedures. A signed distance function (SDF) is computed from the mask to be initially determined. A level set is then utilized to track the deformation of a contour over time. The SDF is computed to represent the level set. Different surfaces and shapes are

analyzed with the level set, and they are then split or merged by the analyzed outcomes. From the image, two different forces consider the deformation of an initial mask. Shrinkage and expansion of the contour are controlled by the forces. The force is computed as follows (17).

$$F_{image} = \int_{inside(C)} (I(x,y) - c_1)^2 dxdy + \int_{outside(C)} (I(x,y) - c_2)^2 dxdy \quad (17)$$

where, C denotes the evolving contour; I denotes the image in which speckle noises are reduced by the SRAD; c_1 denotes the mean of the inside of the contour C, and c_2 denotes the mean of the outside of the contour C. In the equation, the shrinkage is controlled by the first term while the expansion is controlled by the second term. By minimizing F_{image}, the boundary of a target object is obtained in the image. When the contour reaches the boundary of the object, the shrinking and expansion forces are balanced, and thus the F_{image} becomes minimal and stops the deformation of the contour. The details are as follows: the algorithm minimizes the aforementioned fitting term and a regularizing term such as the length of the contour C and area of the region inside C with (18).

$$F(c_1, c_2, C) = \mu \cdot Length(C) + \nu \cdot Area(inside(C)) + \lambda_1 \int_{inside(C)} (I(x,y) - c_1)^2 dxdy + \lambda_2 \int_{outside(C)} (I(x,y) - c_2)^2 dxdy \quad (18)$$

where, $\mu \geq 0$, $\nu \geq 0$, $\lambda_1, \lambda_2 > 0$ are fixed parameters, and the parameters are typically fixed as $\lambda_1 = \lambda_2 = 1$ and $\nu = 0$. The minimization problem can be redefined by the Mumford–Shah function for segmentation as (19).

$$F^{MS}(I, C) = \mu \cdot Length(C) + \lambda \int_{\Omega} |I_0(x,y) - I(x,y)|^2 dxdy + \int_{\Omega/C} |\nabla I(x,y)|^2 dxdy \quad (19)$$

where, I_0 denotes an image for segmentation; C is the contour; Ω denotes the domain of the image, and μ and λ denote positive parameters that affect the quality of segmentation. By smoothing the regions with sharp boundaries in the image I_0, minimization of this function is accomplished, and the solution image I (which is the smoothed image of I_0) follows. Therefore, in this active contour model, the contour C is determined by searching for I, the optimal approximation of I_0, which assumes only two values as (20) with one edge C.

$$I = \begin{cases} mean(I_0) & inside\ C \\ mean(I_0) & outside\ C \end{cases} \quad (20)$$

The problem is represented using the level set method. The contour $C \subset \Omega$ is reformulated by the zero-level set of the Lipschitz function $\phi : \Omega \longrightarrow \mathbb{R}$ as (21)

$$C = \{(x,y) \in \Omega : \phi(x,y) = 0\} \quad (21)$$

For the level set formulation of the active contour model, the unknown variable C is replaced by an unknown variable ϕ. Using the Heaviside function H, the energy term $F(c_1, c_2, \phi)$ is expressed as (22)

$$\begin{aligned} &F(c_1, c_2, \phi) \\ &= \mu \int_{\Omega} \delta(\phi(x,y)) |\nabla \phi(x,y)| dxdy \\ &\quad + \lambda \int_{\Omega} |I(x,y) - c_1|^2 H(\phi(x,y)) dxdy \\ &\quad + \lambda \int_{\Omega} |I(x,y) - c_2|^2 (1 - H(\phi(x,y))) dxdy \end{aligned} \quad (22)$$

Additionally, given image I, the solution of the model is expressed as (23)

$$u(x,y) = c_1 H(\phi(x,y)) + c_2 (1 - H(\phi(x,y))) \quad (23)$$

In order to minimize the energy term $F(c_1, c_2, \phi)$, c_1, c_2 and ϕ are determined where the derivative of F becomes zero. Here, $c_1(\phi)$, $c_2(\phi)$ and ϕ can be updated recursively with (24)-(26).

$$c_1(\phi) = \frac{\int_{\Omega} u_0(x,y) H(\phi(x,y)) dxdy}{\int_{\Omega} H(\phi(x,y)) dxdy} \quad (24)$$

$$c_2(\phi) = \frac{\int_{\Omega} u_0(x,y) (1 - H(\phi(x,y))) dxdy}{\int_{\Omega} (1 - H(\phi(x,y))) dxdy} \quad (25)$$

$$\frac{\partial \phi}{\partial t} = \delta(\phi) \left[I \cdot div\left(\frac{\nabla \phi}{|\nabla \phi|} \right) - \lambda (I_0 - c_1)^2 + \lambda (I_0 - c_2)^2 \right] \quad (26)$$

If the solution is stationary, the recursion then stops.

C. EVALUATION OF THE 3D ULTRASOUND IMAGING PLATFORM AND ALGORITHM

In order to evaluate the performance of the 3D ultrasound imaging platform with the proposed algorithm for the 3D segmentation, we constructed rotator cuff tear-mimicking phantoms, as shown previously [38]. The phantom consists of a normal soft tissue-mimicking region and rotator cuff tear-mimicking region (Fig. 5). The soft tissue-mimicking region exhibits a Young's modulus of 3 kPa, and this is similar to the Young's modulus of normal tissues in the shoulder. Conversely, the rotator cuff tear-mimicking region was

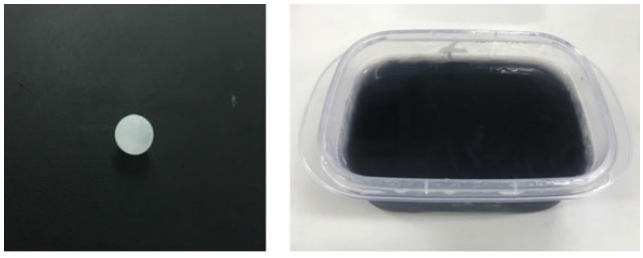

(a) (b)

FIGURE 5. Rotator cuff tear-mimicking phantoms: (a) rotator cuff tear-mimicking region (b) soft tissue-mimicking region.

constructed by filling degassed water into the latex, thereby resulting in hypoechoic regions in an ultrasound image. It is noted that the rotator cuff tear regions typically exhibit hypoechoic rather than normal regions in an ultrasound image of the shoulder [39]. The volumes of the rotator cuff tear regions are 0.2, 0.4, 0.6, and 0.8 ml because the typical volume of rotator cuff tear regions range from 0.15 to 0.80 ml [39]. The volumes were estimated by measuring the water weight and density in the latex.

D. CLINICAL EXPERIMENT

A clinical trial was conducted at Daegu Catholic University Hospital to evaluate the performance of the developed system and algorithm in the detection of rotator cuff regions. Ultrasound images of rotator cuff tear regions of fifteen patients were obtained using the system, and this is followed by 3D segmentation of the rotator cuff regions of the shoulders using the developed algorithm. Rotator cuff disease in the patients was confirmed by two different medical doctors. The clinical trial was approved by the Institutional Review Boards of DCUH. The trials were performed following the relevant guidelines and regulations, and informed consent was obtained from the participants.

E. QUANTITATIVE EVALUATION OF THE DEVELOPED ALGORITHM

For the quantitative analysis of the developed algorithm, the Dice coefficient (DC), Hausdorff distance (HD), and volumetric similarity (VS) were obtained. The Dice coefficient is used as an indicator for the evaluation of accuracy in segmentation. The value between the segmented result and ground truth is obtained with (27),

$$DC_i = \frac{2 \times Area\ of\ Intersection}{Area\ of\ segmented\ result + Area\ of\ ground\ truth} \tag{27}$$

where i denotes the frame number, and the Area of Intersection represents the intersected area between the segmented region and the ground truth region. The ground truths were built under the supervision of medical doctors, and the doctors verified. Additionally, the mean of the DC values for each frame sequence is calculated with (28)

$$Average\ DC = \frac{1}{n}\sum_{i=1}^{n} DC_i \tag{28}$$

The average DC value represents the capability of our developed algorithm for 2D segmentation of rotator cuff tear regions. Furthermore, a volume DC was calculated with (29). The volume DC value represents the capability of the algorithm for 3D segmentation of rotator cuff tear regions.

$$volume\ DC = \frac{2 \times volume\ of\ Intersection}{volume\ of\ segmented\ result + volume\ of\ ground\ truth} \tag{29}$$

The HD measures the similarity of the two sets, which are formed by voxels of the segmented region and ground truth region, in a metric sense. Thus, the lower the HD, the more alike the two sets. The HD is obtained with (30)

$$HD = \max_{a\in A}\{\min_{b\in B}\{d(A,B)\}\} \tag{30}$$

where, a denotes the voxels in the segmented region A and b denotes the voxels in the ground truth region B.

Further, the volume of the segmented region and ground truth are calculated if a volume of one voxel is known. The platform is evaluated using the RCT-mimicking phantom of pre-determined volumes, and thus estimation of the volume is also significant for the evaluation. In the obtained 2D US images, the size of the pixel is $74\mu m \times 53\mu m$, and the size is determined by dividing the actual length of the image by the number of pixels. Similarly, in the reconstructed 3D US images, the length of the voxel (which is an extension of the pixel) was calculated as $110\mu m$, and the 2D images and 3D images were calculated after interpolation. Thus, the volume of a single voxel is $433\mu l$ ($74\mu m \times 53\mu m \times 110\mu m$).

A quantitative comparison of the volumes is required after estimation of the volume of the segmented and ground truth region. Thus, the VS is a proper metric for the purpose. The VS is defined as the absolute volume difference divided by the sum of ground truth volume and segmented volume. It is obtained with (31).

$$VS = 1 - \frac{|volume\ of\ ground\ truth - volume\ of\ segmented\ result|}{volume\ of\ ground\ truth + volume\ of\ segmented\ result} \tag{31}$$

III. RESULTS

A. EVALUATION OF THE PERFORMANCE OF THE 3D IMAGING PLATFORM

In the study, 3D images of a commercial phantom (Model 040GSE, CIRS Inc., Norfolk, VA, USA) were obtained via the 3D ultrasound imaging platform. A 3D image set and the associated 3D reconstructed image are shown in Fig. 6. The 3D image set is shown in Fig. 6(a). The images at different depths in the elevation direction are shown in Fig. 6(b).

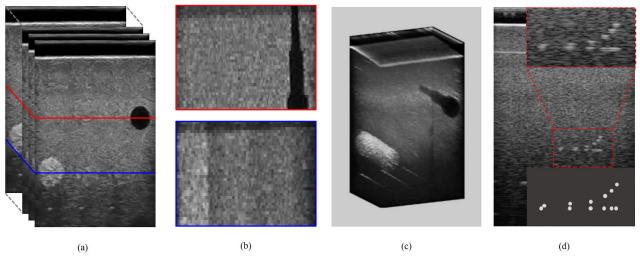

FIGURE 6. Phantom image obtained via the 3D ultrasound imaging system: (a) a 3D image set, (b) sectioned images in the elevation direction, (c) 3D reconstructed image of a commercial phantom, and (d) axial and lateral resolution of the system.

The darkest regions indicate anechoic regions in the phantom. The brighter regions represent hyperechoic regions in the phantom. Figure 6(c) shows the 3D image constructed from the 3D image set. The field of view of the 3D image is 38 mm×50 mm×56 mm, and this is suitable for the imaging of rotator cuff tear regions in the shoulder. Furthermore, the axial and later resolution of the system was investigated via imaging resolution targets with a diameter of 80 μm. The wire targets are placed axially and laterally with certain regular distances at depths of 3 cm. The resolution of the system was determined as the minimum distance of the wire targets that can be imaged separately using the system. Thus, the system offered an axial resolution of 250 μm and a lateral resolution of 1 mm. In the magnified image (Fig. 6(d), above inset), with the graphical description of the actual targets as a reference (Fig. 6(d), bottom inset), it was observed that two targets at the left-most location were distinguishable in the axial direction whereas two targets at the right-most below location were not clearly distinguishable in the lateral direction.

B. FREQUENCY COMPOUNDING EFFECTS ON THE REGIONS OF INTEREST IN AN ULTRASOUND IMAGE

A frequency compounding technique was applied to an ultrasound image to decrease speckle noise and to improve the contrast-to-noise ratio (CNR) of an ultrasound image in the 3D segmentation of the rotator cuff tear regions. In order to evaluate the effects of the frequency compounding on the ultrasound image, the speckle SNRs and CNRs of the ultrasound image after 2-band and 4-band frequency compounding were compared to those of the corresponding original ultrasound image. Figure 6 shows the ultrasound image of a commercial phantom before and after the frequency compounding. After the 2-band and 4-band frequency compounding of the image, speckles in the ultrasound image are significantly reduced as shown in Figs. 7(b) and (c). The speckle SNR of the ultrasound image was improved by 2.1975 from 1.898 due to the 2-band frequency compounding whereas it was improved by 2.4999 from 1.898 after the 4-band frequency compounding (Table. 1). Additionally, the CNRs of the ultrasound image before and after frequency compounding were compared. Two ROIs should be specified to estimate the CNR. In the ultrasound images, regions

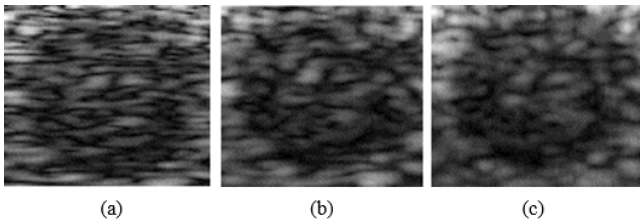

FIGURE 7. Comparisons of ultrasound images before and after frequency compounding (a) original ultrasound image, (b) ultrasound image after 2-band frequency compounding, and (c) ultrasound image after 4-band frequency compounding.

TABLE 1. Speckle SNR and CNR of ultrasound images before and after 2 sub-band frequency compounding and 4 sub-band frequency compounding of the images.

	Speckle SNR	CNR
original	1.898	0.557
2-band FC	2.195	0.622
4-band FC	2.499	0.789

inside and outside of the anechoic region are specified as the ROIs. Thus, the CNRs of the ultrasound images after 2-band and 4-band frequency compounding were measured as 0.622 and 0.789, respectively, whereas the CNR of the original ultrasound image corresponded to 0.557. The CNRs of the ultrasound image were significantly improved via frequency compounding.

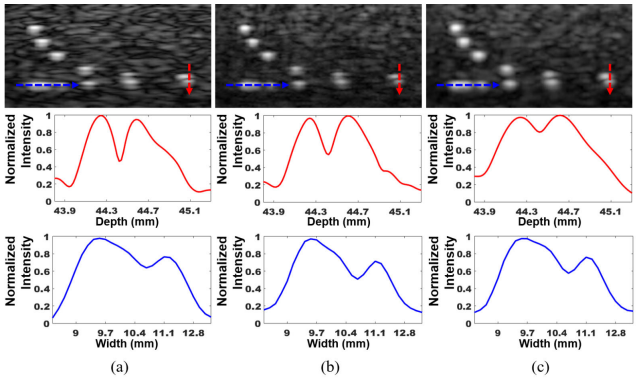

FIGURE 8. Ultrasound images of resolution target regions of the commercial phantom before and after frequency compounding with different number of bands (a) Original ultrasound and intensity profiles along the targets for examination of the lateral and axial resolutions (b) Ultrasound image after 2-band frequency compounding and intensity profiles along the targets for examination of lateral and axial resolutions (c) Ultrasound image after 4-band frequency compounding and intensity profiles along targets for examination of lateral and axial resolutions. The red dotted rectangle indicates two targets separately located within a distance of 250 μm in the axial direction.

Additionally, the effects of the frequency compounding on the axial and lateral resolution were examined. Figure 8 shows the ultrasound images of the resolution target regions before and after the 2-band [Fig. 8(b)] or 4-band [Fig. 8(c)] frequency compounding. As shown in Fig. 8, the axial resolution was degraded due to frequency compounding. The axial resolution slightly worsened because the sub-band number for the frequency compounding increased (Fig. 8, middle). In the 4-band frequency compounding image, two targets located within a distance of 250 μm in the axial direction were discernable albeit not clearly [Fig. 8(c)]. Conversely, the intensity profiles of the targets as indicated by the blue arrow to investigate changes in the lateral resolution due to the frequency compounding were examined. The results indicated that the lateral resolution was not significantly degraded due to frequency compounding. The results indicate that the frequency compounding significantly decreased the speckle SNR and improved the CNR whereas it slightly degraded

axial resolutions when the number of bands increased in the frequency compounding.

C. 3D SEGMENTATION OF MIMICKED ROTATOR CUFF TEAR REGIONS WITH DIFFERENT VOLUMES

To evaluate the performance of the 3D ultrasound imaging platform with the proposed algorithm for 3D segmentation, we performed 3D imaging of rotator cuff tear-mimicking phantoms with different volumes and then applied the proposed algorithm to the images for 3D segmentation of the mimicked rotator cuff tear regions. The pre-processing affect the US image quality and performance of the segmentation. Thus, the effects of the combinations of the pre-processing methods (FC, SRAD) were quantitatively and qualitatively evaluated via the phantom experiment. An adaptive histogram equalization (AHE) was essentially applied to enhance the image contrast. Frequency compounding was used as 2 sub-band FC and 4 sub-band FC. Furthermore, SRAD was also used. Thus, a total of six pre-processing procedures were compared including combinations involving the absence of each method.

The acquired 3D image and segmented result of the RCT-mimicking phantom in which the volume is 0.6 ml are visualized in 3D as shown in Fig. 9. The segmented RCT region(Fig. 9, right) is the result of a combination of pre-processing methods that results in the optimal performance. More explicit 3D segmented images of other phantoms of different volumes are shown in Fig. 10. The left side of Fig. 10 shows the segmented results of the pre-processing procedure that consists of 2 sub-band FC and SRAD. Conversely, the right side shows the segmented results of the pre-processing procedure without FC and SRAD. The segmented regions (Fig. 10, left side) exhibit good agreement with the manually segmented regions (ground truths), and the pre-processing procedure (2 sub-band FC/SRAD) evidently significantly enhanced the performance of the segmentation.

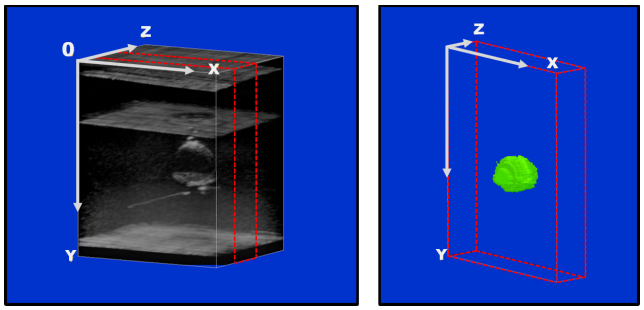

FIGURE 9. 3D reconstructed B-mode image of rotator cuff mimicking phantom with a volume of 0.6 ml and segmented rotator cuff tear-mimicking phantom that is denoted in green.

The average DC, volume DC values, and HDs were compared as shown in Table. 2 for the quantitative analysis of the performance of the pre-processing procedures in the proposed algorithm for the 3D segmentation of RCT regions.

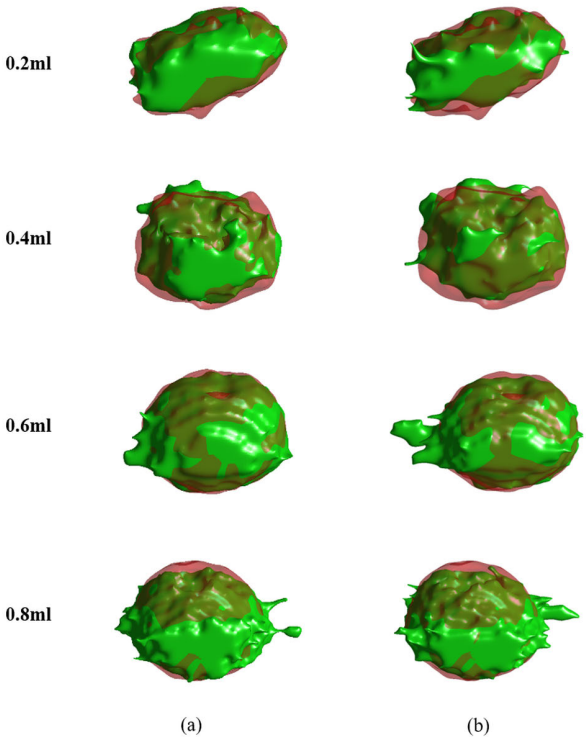

FIGURE 10. 3D segmentation of the mimicked RCT regions with different volumes: Green color denotes the segmentation and transparent red color denotes the ground truth on (a) 3D segmentation with 2-band frequency compounding/SRAD/Active contour and (b) 3D segmentation image with original/Active contour.

Following the application of 2 sub-band FC, the averaged DC and volume DC values increased by 5% when compared to that in absence of FC. The 4 sub-band FC also slightly increased the average DC and volume DC values when compared to the 2 sub-band FC. The HD also decreased with the 2 and 4 sub-band FC. Furthermore, SRAD (which is typically used to suppress speckle noise while preserving edges) was applied to the original US images, two and 4 sub-band images. Specifically, SRAD slightly increased or decreased the performance. Although the effect is slight, the pre-processing procedure of 2 sub-band FC and SRAD resulted in optimal segmentation accuracy among the various combinations. The average DC and volume DC values corresponded to 0.861 and 0.885, respectively, which are approximately 5% higher than the lowest value of those metrics. The HD is 4.96 mm, which is considerably improved when compared to the highest value(5.58 mm) and is similar to the lowest value (4.85 mm).

Furthermore, the volumes of the rotator cuff tear-mimicking phantoms estimated from the ground truths and segmented results were compared with the VS between the ground truths and segmented results (Table. 3). Specifically, we also applied the pre-processing procedure of the two-sub-band FC and SRAD to the images prior to the application of the active contour processing. The VS values for the phantoms at 0.2, 0.4, 0.6, and 0.8 ml are 0.980, 0.891,

TABLE 2. Average DC, volume DC, and HD values of 3D segmentation of the mimicked RCT regions with different volumes by different pre-processing procedures; standard deviations are presented in the parentheses.

Pre-Processing		RCT phantom volume	Average DC	volume DC	HD (mm)
Original	AHE	0.2 ml	0.837	0.863	4.20
		0.4 ml	0.790	0.817	4.51
		0.6 ml	0.894	0.905	4.95
		0.8 ml	0.798	0.824	7.90
		mean	**0.830 (0.047)**	**0.852 (0.041)**	**5.39 (1.70)**
	AHE + SRAD	0.2ml	0.844	0.869	3.88
		0.4 ml	0.762	0.818	5.68
		0.6 ml	0.898	0.913	4.95
		0.8ml	0.786	0.827	7.81
		mean	**0.822 (0.061)**	**0.857 (0.043)**	**5.58 (1.66)**
Two sub-band FC	AHE	0.2 ml	0.882	0.900	4.04
		0.4 ml	0.765	0.808	4.28
		0.6 ml	0.941	0.944	4.95
		0.8 ml	0.825	0.859	7.81
		mean	**0.853 (0.076)**	**0.878 (0.058)**	**4.90 (1.57)**
	AHE + SRAD	0.2ml	0.883	0.903	3.99
		0.4ml	0.785	0.825	4.40
		0.6 ml	0.942	0.947	4.09
		0.8 ml	0.832	0.865	7.37
		mean	**0.861 (0.067)**	**0.885 (0.052)**	**4.96 (1.61)**
Four sub-band FC	AHE	0.2 ml	0.880	0.900	3.59
		0.4 ml	0.790	0.828	4.41
		0.6 ml	0.939	0.949	3.88
		0.8 ml	0.816	0.857	7.53
		mean	**0.856 (0.067)**	**0.883 (0.053)**	**4.85 (1.82)**
	AHE + SRAD	0.2 ml	0.879	0.899	3.62
		0.4 ml	0.783	0.782	4.59
		0.6 ml	0.939	0.948	3.88
		0.8 ml	0.812	0.851	7.57
		mean	**0.853 (0.070)**	**0.870 (0.071)**	**4.91 (1.82)**

TABLE 3. Estimated volumes of the RCT mimicked region and the VSs calculated with the volumes: segmented with a combination that provides the highest average DC value.

RCT-mimicked phantom volume	0.2 ml	0.4 ml	0.6 ml	0.8 ml
Ground truth (ml)	0.162	0.299	0.555	0.889
Ours (ml)	0.156	0.240	0.563	0.849
VS	0.980	0.891	0.993	0.979

0.993, and 0.979, respectively. The results demonstrate that the performance of the 3D ultrasound imaging platform with the proposed algorithm with the pre-processing procedure is sufficiently high such that the algorithm can be used to quantitatively analyze rotator cuff tear regions.

D. 3D SEGMENTATION OF THE ROTATOR CUFF TEAR REGIONS USING THE DEVELOPED ALGORITHM

After evaluation of the performance of the 3D ultrasound imaging platform with the proposed algorithms for the 3D segmentation, a clinical test was conducted at Daegu Catholic University Hospital using the developed platform and algorithms. Participants were preoperative and include a total of 15 patients. A medical doctor obtained the 3D ultrasound images via the platform. The developed algorithms were applied to the 3D ultrasound images to segment the rotator cuff tear regions of the participants. The computation time of the algorithm is less than 1 min for the segmentation of single clinical data.

The obtained 3D image and associated segmented 3D image of rotator cuff tear regions with different views (Case 4) are shown in Fig. 11. Furthermore, to examine the effects of the pre-processing including the frequency compounding and SRAD on 3D segmentation, we compared the 3D segmented images of the rotator cuff tear regions, as obtained by algorithms with (Fig. 12(a)) and without the 2 sub-band frequency compounding and SRAD (Fig. 12(b)), with the 3D ground truth images. The 3D ground truth images were reconstructed using 2D ground truth images. The 3D segmented images (green), as obtained by the algorithms, are presented as overlaid with the 3D ground truths (red)(Fig. 12). Here, it was observed that the 3D segmented images obtained by the algorithm with the 2-band frequency compounding and SRAD were better matched with the 3D ground truths than those by the algorithm without the pre-processing.

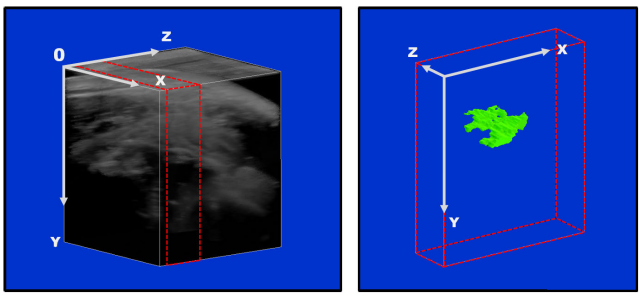

FIGURE 11. 3D reconstructed B-mode image of rotator cuff tear region and segmented rotator cuff tear region denoted in green(Case 4).

For further quantitative analysis of the proposed algorithm, the average and volume DC values and HD, as obtained by the algorithm with different pre-processing procedures, are compared and listed in Table. 4. In a manner similar to the result of the RCT-mimicking phantom experiment, the frequency compounding significantly increased the performance of the segmentation. After 2 sub-band frequency compounding, the average DC and volume DC values increased by 10% when compared to those in the absence of the FC. However, the 4 sub-band FC (which also expected to improve the performance of the segmentation) worsened the performance when compared to the 2 sub-band FC even it is better than

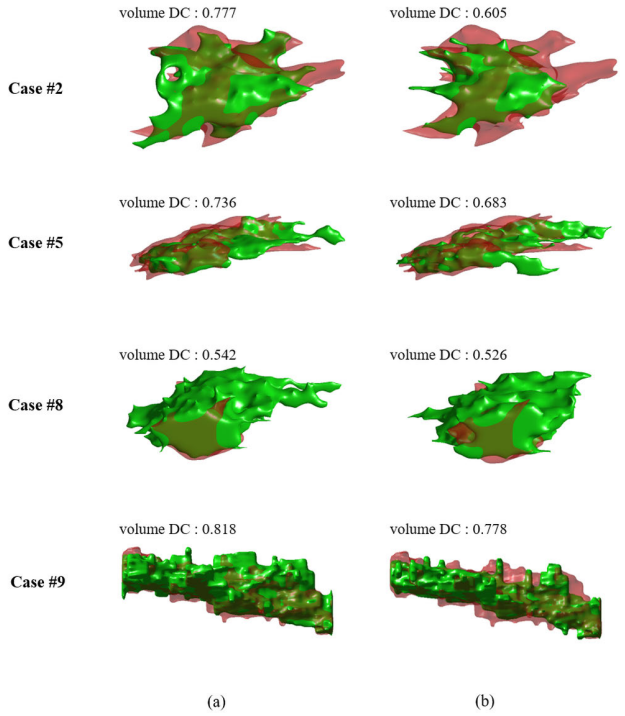

FIGURE 12. Comparisons of 3D segmented images of rotator cuff tear regions as obtained by the developed algorithm with 3D ground truths that are constructed with 2D ground truth images: (a) 3D segmented images obtained by the developed algorithm (2-band frequency compounding/SRAD/Active contour) and (b) 3D segmentation images obtained via an active contour technique without the preprocessing that includes the 2-band frequency compounding/SRAD. Green color denotes 3D segmented images whereas the red color denotes ground truths.

TABLE 4. Mean of Average DC, volume DC, and HD values of the 3D segmentation of the RCT regions for all cases with the different pre-processing procedures; standard deviations are presented in the parenthesis.

Pre-Processing		Average DC	volume DC	HD(mm)
Original	AHE	0.551 (0.165)	0.624 (0.157)	6.43 (2.34)
	AHE+SRAD	0.576 (0.155)	0.646 (0.152)	6.46 (2.01)
Two sub-band FC	AHE	0.652 (0.092)	0.704 (0.090)	5.82 (1.74)
	AHE + SRAD	0.663 (0.085)	0.723 (0.081)	5.68 (1.95)
Four sub-band FC	AHE	0.628 (0.108)	0.689 (0.113)	5.97 (2.56)
	AHE + SRAD	0.611 (0.113)	0.667 (0.124)	5.98 (2.70)

TABLE 5. Volume similarity(VS) and volume DC values for different volumes segmented by the proposed algorithm with the 2 sub-band FC/SRAD/AHE.

Estimated volume	< 0.2ml	< 0.4ml	> 0.4ml
number of cases	10	3	2
mean of VSs	0.839	0.873	0.985
mean of volume DCs	0.708	0.711	0.815

that in the absence of FC. The results indicate that the 4 sub-band FC deteriorated the axial resolution of US images, as shown in Fig. 8. Although the deterioration did not affect the phantom experiment in which the boundary of the mimicked-RCT region is clear, it resulted in worse performance in the clinical trial in which the RCT region exhibited a more vague boundary that easily collapsed with pre-processing.

The application of SRAD was also evaluated. In a manner similar to the result of the phantom experiment, SRAD decreased the performance of the original and 4 sub-band FC images and increased the performance of the 2 sub-band FC images. Therefore, when the 2 sub-band frequency compounding and SRAD techniques were sequentially applied to ultrasound images before application of the active contour technique, the average DC and volume DC values were the highest and the HD corresponded to the lowest value. The average DC value was 0.663, which is 11% higher than that obtained with the original ultrasound images. The volume DC value was 0.723, which is 10% higher than that obtained with no pre-processing methods with the exception of AHE. The HD was 5.68 mm, which is considerably lower than the largest value of 6.46 mm.

Additionally, the volumes for all the cases were calculated using the segmented results of the proposed algorithm that consists of the pre-processing procedure (2 sub-band FC/SRAD/AHE). Subsequently, volume similarity (VS) was calculated for all the cases, and the VSs were categorized via their volumes (lower than 0.2 ml, lower than 0.4 ml, larger than 0.4 ml). The mean of the VSs for each categorized group was given with the mean of volume DCs(Table. 5). The group of the cases with volume exceeding 0.4 ml exhibited higher VSs and volume DCs than the groups of lower volume cases. Decreases in the volume decreased the accuracy(VS, volume DC). The mean and standard deviation of the total VSs were 0.865 ± 0.106. These results suggest that the 3D ultrasound imaging platform with the proposed algorithm with the pre-processing combination of 2 sub-band frequency compounding, SARD, and AHE exhibits potential for 3D quantitative analysis of rotator cuff tear regions.

For further evaluation of the performance of the developed algorithm, the segmentation outcomes obtained with clinical data via algorithms based on watershed, region growing, and active contour(centroid) were compared with the results of our developed algorithms (Table. 6). With respect to the watershed, region growing, and active contour(centroid), the pre-processing combination (2 sub-band FC/SRAD) was applied in a manner similar to developed algorithm before the segmentation step. Specifically, the active contour(centroid)-based algorithm initializes masks by a centroid (center of mass) of a previous segmented frame, which is a conventional

TABLE 6. Comparisons of average and volume DCs obtained using the proposed algorithm (underlined) and other conventional algorithms.

Method	Watershed	Region growing	Active contour (centroid)	Active contour (randomly seed)
Average DC	0.374 (0.176)	0.374 (0.205)	0.614 (0.107)	0.663 (0.085)
volume DC	0.428 (0.210)	0.442 (0.230)	0.677 (0.105)	0.723 (0.081)

method for 3D segmentation [30]–[32]. Conversely, the proposed algorithm randomly generates masks on a subsequent frame based on the segmented contour of the previous frame and select optimal mask for the subsequent frame. The randomly generated masks in the active contour processing resulted in a more robust segmentation of tumors than the generated mask at a centroid.

Thus, the watershed-based algorithm exhibited an average DC value of 0.374 and a volume DC value of 0.428. The watershed-based algorithm exhibited over-segmentation of the rotator cuff tear regions. The results indicate that the rotator cuff tear and the bone regions were connected after the watershed transformation in several images. Conversely, the region growing-based algorithm exhibited an average DC value of 0.374 and a volume DC value of 0.442. The findings reveal that when ultrasound images exhibit ambiguous boundaries on rotator cuff tear regions or low-intensity regions on their boundaries, and the growing regions penetrated into unwanted regions via the low-intensity regions and ambiguous boundaries. In contrast, given the superiority of active contour that detected an overall edge contour of the target object and also controlled the smoothness of the contour, and thus the active contour-based algorithm exhibited significantly increased accuracy with an average DC value of 0.614 and volume DC value of 0.677. However, the active contour-based algorithm occasionally exhibited the wrong initialization of masks during the segmentation of the RCT region in 3D US images. Eventually, the segmentation of the rest of the 3D image after the inaccurate initialization failed. This is also due to severely vague boundary and irregular shape of the RCT region. The developed algorithm enhanced accuracy with randomly seeded masks for avoiding the wrong initialization. Thus, it resulted in the highest average DC value of 0.663 in the 3D segmentation of rotator cuff tear regions. Furthermore, it suggests that the developed algorithm outperformed the previous watershed, region growing-based algorithms, and the active contour(centroid)-based algorithm in the segmentation of rotator cuff tear regions.

IV. DISCUSSION

As previously mentioned, the quantitative analysis of rotator cuff tear regions in 3D aids in the determination of treatment plans and monitoring of treatment efficacy. In the study, for the 3D analysis of rotator cuff tear region, we developed a wide-field 3D ultrasound imaging platform exploiting conventional 2D US imaging system with linear step motor, DAQ board, and 3D-printed scanning apparatus. Additionally, for providing volumetric information of rotator cuff tear regions, a semi-automatic 3D segmentation algorithm was developed with an extension of the conventional 2D segmentation algorithm (Chan-Vese active contour) using frequency compounding and SRAD as pre-processing. The capability of the developed platform (including the developed algorithm) in terms of the quantitative analysis of the rotator cuff tear region was demonstrated via the RCT-mimicking phantom experiment and clinical trials (15 patients).

In the wide-field 3D US imaging platform, the DAQ board (which was used in the study (USB6341, National Instrument, USA)) can be replaced with a cheaper board that exhibits the same function. Thus, the cost for the development using the conventional 2D US imaging system (DAQ board with a cheaper price: 200$, linear step motor: 200$) can be lower than the commercial 3D US system with 2D matrix array transducer as well as the conventional MRI. Additionally, the developed platform offered a 3D image with a larger FoV (maximum: 38 mm×90 mm×56 mm) than the 2D matrix array transducer, and thus it is more suitable for analysis of rotator cuff tears. It is noted that the field of view is sufficient to image rotator cuff tear regions in 3D. Errors or artifacts can exist in the reconstructed 3D image which aroused due to the motion of the probe or patient. However, the single scanning using the platform is sufficiently rapid (10 s) to avoid the motions of a patient for a while. Thus, errors and artifacts due to the movement of a patient can be avoided. Specifically, we did not observe any significant artifacts due to the movements of patients in the study. The time is significantly shorter than the time for scanning using MRI (30 min). Furthermore, the platform was configured using a conventional 2D US system, which was widely used in the clinic. It is noted that the use of the platform does not require anything specific such as calibration and tedious setting. Thus, even clinicians who are novices to the platform can easily adapt to the platform.

In the semi-automatic 3D segmentation algorithm, the proposed approach with randomly seeded masks was attempted to improve the prior approach which utilized the center of mass as an initial mask [30]–[32] for the extension of the 2D segmentation algorithm to segment a 3D object. The performance of the new approach exhibited better performance than the prior approach and other algorithms based on conventional segmentation methods (watershed, region growing) (Table. 6). Furthermore, frequency compounding and SRAD were applied to enhance the quality of US images before the segmentation step. Specifically, frequency compounding in which the effect on the segmentation is not sufficiently examined to-date, to the best of the author's knowledge [40], was additionally evaluated using a commercial phantom(Model 040GSE, CIRS Inc., Norfolk, VA, USA), and its effect was demonstrated with increases in SNR and CNR. However, it worsened the axial resolution (Fig. 7, Fig. 8, Table. 1) as proved previously [34]. The degradation in axial resolution makes it difficult to detect the boundary of the RCT region

and leads to low accuracy of the segmentation. Eventually, it can lead to a decrease in the accuracy of diagnosis. However, a trade-off exists for high performance of the segmentation between speckle noise and axial resolution while varying the number of sub-bands. Specifically, in the clinical trials, the 2 sub-band frequency compounding exhibited better performance in the 3D segmentation than the 4 sub-band frequency compounding and absence of the frequency compounding (Table. 4).

Thus, FC considerably improved the performance of the segmentation when compared to SRAD, which is conventionally utilized to eliminate speckle noise. And, SRAD did not show significant improvement in the study (Table. 2, Table. 4). Although the effect of SRAD is negligible, the pre-processing procedure that consists of 2 sub-band FC and SRAD resulted in the highest accuracy as demonstrated with average DC, volume DC, and HD. However, the performance of the segmentation was considerably lower in the clinical trial when compared to the phantom experiment. This is because the boundaries of the rotator cuff tear regions were significantly more ambiguous than those of the RCT-mimicking phantoms. Hence, the developed algorithm exhibited good performance in the 3D segmentation of rotator cuff tear regions.

Conversely, as shown in Table. 5, the RCT regions of lower volume($<$0.4 ml) resulted in lower accuracy of the segmentation than the RCT regions of a larger volume($>$0.4 ml)(Table. 5). In the algorithm, a region of interest was not specified although an overall US image was processed, and thus a small rotator cuff tear (which is relatively lower than the image) was not accurately detected. Nevertheless, the mean of VS for the 3D segmented rotator cuff tear regions by the developed algorithm is 0.865, and this can be sufficiently high for the quantification of rotator cuff tear regions. However, in the phantom experiment, the degradation based on the volume was not observed (Table. 3) given the clearer boundary and spherical shape of the mimicked-RCT region that maximized the capability of being detected and the size of the region (Fig. 5, Fig. 9). However, the phantoms of real volumes (which are less than 0.6 ml) exhibited slightly lower volumes, as estimated from the segmented results and ground truths, when compared to the real volumes of each. This can be due to the limited lateral and axial resolutions of the 3D ultrasound imaging platform. It is improved by the development of a high-frequency ultrasound imaging platform.

The wide-field 3D US imaging platform with the semi-automatic 3D segmentation algorithm exhibited its capability to provide readily available quantitative analysis of rotator cuff tear regions with cost and time savings. Furthermore, the platform with the algorithm satisfied doctors with the necessity to understand better spatial information in the diagnosis of RCT for better treatment planning. Although the platform with the algorithm enabled more accurate 3D analysis of rotator cuff tear region with wider FoV than conventional 2D and 3D US systems, the MRI can exhibit superior performance in terms of the proposed system because it offers better resolution and sensitivity (Fig. 13). Nevertheless, previous studies suggested that MRI and US exhibit comparable accuracy in the diagnosis of a rotator cuff tear. Thus, in this regard, the platform can aid in the diagnosis and monitoring of the rotator cuff tear and especially with accurate visible 3D information, good accessibility, time and cost efficiency, and easy repeatability.

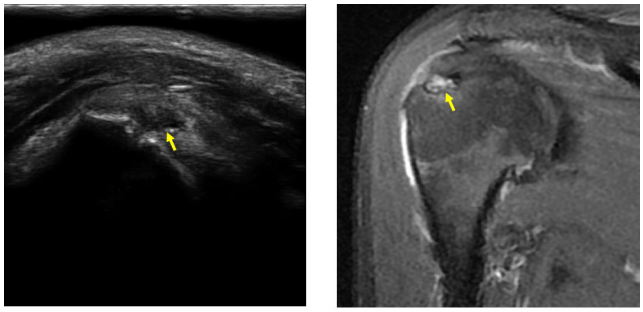

FIGURE 13. US image of the rotator cuff tear region and corresponding MRI image; yellow arrows delineate the RCT region.

The linear scanning method utilized in the study enabled simple and reliable scan conversion with the accurate position information of the transducer. The simplicity can be demonstrated without the need for a unique algorithm or high computational cost. Additionally, as shown in Table. 3, real volume and estimated volumes are not significantly different, and it proves the reliability. However, in the clinical trial, a potential angle-dependent artifact existed, and this is termed as anisotropy. When the ultrasound beam is incident on a tendon, the organized fibrils can reflect a majority of the beam in a direction away from the transducer. This results in the transducer not receiving the returning echo, and this can be assumed as hypoechoic area and indicates a tear. In the study, the artifact anisotropy was avoided due to the doctor's effort wherein the artifact did not occur due to an arbitrary optimal position of imaging. Hence, this can cause operator variability in the platform. Therefore, the development of a credible novel free-hand scanning method or the application of ultrafast imaging (which can image a single frame with beams of various incident angles) can avoid anisotropy and improvement of operator-reliability. Additionally, a novel free-hand scanning method can aid in the improvement of the platform's usability by a doctor.

Furthermore, inter/intra-variability can exist when using the semi-automatic 3D segmentation algorithm because there exists an intervention by a doctor even if it is only once, and the intervention can be affected by the doctor's subjective view. It can improve with the development of the fully-automatic segmentation algorithm using a deep-learning approach. Furthermore, when a large set of clinical data is ready, the deep-learning approach can make the segmentation algorithm more accurate and robust. This can constitute the focus of a future study with improvements in the 3D US platform.

V. CONCLUSION

In the study, we developed a wide-field 3D imaging platform with the semi-automatic segmentation algorithm that can provide a 3D quantitative analysis of rotator cuff tears in a short image acquisition time with less cost. The platform is useful in terms of developing a platform for 3D quantitative analysis based on readily available imaging modality, i.e., ultrasound imaging. Thus, the platform can aid in the analysis of rotator cuff tears, which was previously qualitatively diagnosed based on the experience of a doctor. Eventually, it is expected to quantitatively lead to better treatment plans and monitoring treatment efficacy for rotator cuff disease.

Furthermore, the platform exhibits the potential to further serve as a platform for image vascularity (which is useful information for monitoring treatment efficacy) with anatomic information in 3D via the application of ultrasound Doppler or photoacoustic imaging. This will be examined in a future study.

ACKNOWLEDGMENT

The authors thank all the participants. *(Moon Hwan Lee and Jun-Young Kim contributed equally to this work.)*

REFERENCES

[1] S. Tempelhof, S. Rupp, and R. Seil, "Age-related prevalence of rotator cuff tears in asymptomatic shoulders," *J. Shoulder Elbow Surgery*, vol. 8, no. 4, pp. 296–299, Jul. 1999.

[2] S. E. Dalton, "The conservative management of rotator cuff disorders," *Rheumatology*, vol. 33, no. 7, pp. 663–667, 1994.

[3] A. N. Fotiadou, M. Vlychou, P. Papadopoulos, D. S. Karataglis, P. Palladas, and I. V. Fezoulidis, "Ultrasonography of symptomatic rotator cuff tears compared with mr imaging and surgery," *Eur. J. Radiol.*, vol. 68, no. 1, pp. 174–179, 2008.

[4] C. A. Fischer, M.-A. Weber, C. Neubecker, T. Bruckner, M. Tanner, and F. Zeifang, "Ultrasound vs. MRI in the assessment of rotator cuff structure prior to shoulder arthroplasty," *J. Orthopaedics*, vol. 12, no. 1, pp. 23–30, Mar. 2015.

[5] M. J. C. M. Rutten, J. M. P. Collins, B. J. Maresch, J. H. J. M. Smeets, C. M. M. Janssen, L. A. L. M. Kiemeney, and G. J. Jager, "Glenohumeral joint injection: A comparative study of ultrasound and fluoroscopically guided techniques before MR arthrography," *Eur. Radiol.*, vol. 19, no. 3, pp. 722–730, Mar. 2009.

[6] A. Teng, F. Liu, D. Zhou, T. He, Y. Chevalier, and R. M. Klar, "Effectiveness of 3-dimensional shoulder ultrasound in the diagnosis of rotator cuff tears: A meta-analysis," *Medicine*, vol. 97, no. 37, Sep. 2018, Art. no. e12405.

[7] S. Saraya and R. El Bakry, "Ultrasound: Can it replace MRI in the evaluation of the rotator cuff tears?" *Egyptian J. Radiol. Nucl. Med.*, vol. 47, no. 1, pp. 193–201, Mar. 2016.

[8] W. D. Middleton, W. T. Payne, S. A. Teefey, C. F. Hildebolt, D. A. Rubin, and K. Yamaguchi, "Sonography and MRI of the shoulder: Comparison of patient satisfaction," *Amer. J. Roentgenol.*, vol. 183, pp. 1449–1452, Nov. 2004.

[9] J.-S. Roy, C. Braën, J. Leblond, F. Desmeules, C. E. Dionne, J. C. MacDermid, N. J. Bureau, and P. Frémont, "Diagnostic accuracy of ultrasonography, MRI and MR arthrography in the characterisation of rotator cuff disorders: A systematic review and meta-analysis," *Brit. J. Sports Med.*, vol. 49, no. 20, pp. 1316–1328, Oct. 2015.

[10] S. A. Teefey, D. A. Rubin, W. D. Middleton, C. F. Hildebolt, R. A. Leibold, and K. Yamaguchi, "Detection and quantification of rotator cuff tears: Comparison of ultrasonographic, magnetic resonance imaging, and arthroscopic findings in seventy-one consecutive cases," *J. Bone Joint Surg.-Amer. Volume*, vol. 86, no. 4, pp. 708–716, Apr. 2004.

[11] C.-Y. Chang, S.-F. Wang, H.-J. Chiou, H.-L. Ma, Y.-C. Sun, and H.-D. Wu, "Comparison of shoulder ultrasound and MR imaging in diagnosing full-thickness rotator cuff tears," *Clin. Imag.*, vol. 26, no. 1, pp. 50–54, Jan. 2002.

[12] J. O. de Jesus, L. Parker, A. J. Frangos, and L. N. Nazarian, "Accuracy of MRI, MR arthrography, and ultrasound in the diagnosis of rotator cuff tears: A meta-analysis," *Amer. J. Roentgenol.*, vol. 192, no. 6, pp. 1701–1707, Jun. 2009.

[13] T. O. Smith, T. Back, A. P. Toms, and C. B. Hing, "Diagnostic accuracy of ultrasound for rotator cuff tears in adults: A systematic review and meta-analysis," *Clin. Radiol.*, vol. 66, no. 11, pp. 1036–1048, Nov. 2011.

[14] Q. Huang and Z. Zeng, "A review on real-time 3D ultrasound imaging technology," *BioMed Res. Int.*, vol. 2017, Mar. 2017.

[15] Q.-H. Huang, Z. Yang, W. Hu, L.-W. Jin, G. Wei, and X. Li, "Linear tracking for 3-D medical ultrasound imaging," *IEEE Trans. Cybern.*, vol. 43, no. 6, pp. 1747–1754, Dec. 2013.

[16] F. Mohamed and C. Vei Siang, "A survey on 3D ultrasound reconstruction techniques," in *Artificial Intelligence—Applications in Medicine and Biology*. London, U.K.: IntechOpen, 2019.

[17] T. A. Wallny, I. Theuerkauf, R. L. Schild, L. Perlick, and D. S. Bertelsbeck, "The three-dimensional ultrasound evaluation of the rotator cuff—An experimental study," *Eur. J. Ultrasound*, vol. 11, no. 2, pp. 41–135, 2000. [Online]. Available: https://www.ncbi.nlm.nih.gov/pubmed/10781662

[18] C. D. Ainsworth, C. C. Blake, A. Tamayo, V. Beletsky, A. Fenster, and J. D. Spence, "3D ultrasound measurement of change in carotid plaque volume a tool for rapid evaluation of new therapies," *Stroke*, vol. 36, no. 9, pp. 1904–1909, 2005. [Online]. Available: https://www.ahajournals.org/doi/abs/10.1161/01.STR.0000178543.19433.20

[19] R.-F. Chang, W.-J. Wu, W. K. Moon, W.-M. Chen, W. Lee, and D.-R. Chen, "Segmentation of breast tumor in three-dimensional ultrasound images using three-dimensional discrete active contour model," *Ultrasound Med. Biol.*, vol. 29, no. 11, pp. 1571–1581, Nov. 2003.

[20] Q. Huang, B. Xie, P. Ye, and Z. Chen, "3-D ultrasonic strain imaging based on a linear scanning system," *IEEE Trans. Ultrason., Ferroelectr., Freq. Control*, vol. 62, no. 2, pp. 392–400, Feb. 2015. [Online]. Available: https://www.ncbi.nlm.nih.gov/pubmed/25643088

[21] A. Landry, J. D. Spence, and A. Fenster, "Quantification of carotid plaque volume measurements using 3D ultrasound imaging," *Ultrasound Med. Biol.*, vol. 31, no. 6, pp. 751–762, Jun. 2005.

[22] *Quantifying Full-Thickness Rotator Cuff Tears Using 3D Ultrasound*, document ECR 2010/c-2231/, EPOS, 2010.

[23] P.-W. Hsu, R. Prager, A. Gee, and G. Treece, *Freehand 3D Ultrasound Calibration: A Review*, vol. 1. Jan. 2009, pp. 47–84.

[24] D. F. Leotta and R. W. Martin, "Three-dimensional ultrasound imaging of the rotator cuff: Spatial compounding and tendon thickness measurement," *Ultrasound Med. Biol.*, vol. 26, no. 4, pp. 509–525, May 2000.

[25] D. Montagnon, "Quantifying full-thickness rotator cuff tears using 3D ultrasound," in *Proc. Eur. Congr. Radiol.*, 2010. pp. 47–84.

[26] K. Horsch, M. L. Giger, L. A. Venta, and C. J. Vyborny, "Automatic segmentation of breast lesions on ultrasound," *Med. Phys.*, vol. 28, no. 8, pp. 1652–1659, 2001.

[27] D. Zhang, Y. Liu, Y. Yang, M. Xu, Y. Yan, and Q. Qin, "A region-based segmentation method for ultrasound images in HIFU therapy," *Med. Phys.*, vol. 43, no. 6, pp. 2975–2989, May 2016.

[28] Y.-L. Huang and D.-R. Chen, "Watershed segmentation for breast tumor in 2-D sonography," *Ultrasound Med. Biol.*, vol. 30, no. 5, pp. 625–632, May 2004.

[29] K. Saini, M. Rohit, and M. L. Dewal, "Ultrasound imaging and image segmentation in the area of ultrasound: A review," *Int. J. Adv. Sci. Technol.*, vol. 24, pp. 41–60, Nov. 2010.

[30] P. Poudel, A. Illanes, C. Arens, C. Hansen, and M. Friebe, "Active contours extension and similarity indicators for improved 3D segmentation of thyroid ultrasound images," in *Medical Imaging 2017: Imaging Informatics for Healthcare, Research, and Applications*, vol. 10138. 2017, p. 1013803, doi: 10.1117/12.2254029.

[31] E. Karami, M. Shehata, P. McGuire, and A. Smith, "A semi-automated technique for internal jugular vein segmentation in ultrasound images using active contours," in *Proc. IEEE-EMBS Int. Conf. Biomed. Health Informat. (BHI)*, Feb. 2016, pp. 184–187.

[32] P. Poudel, C. Hansen, J. Sprung, and M. Friebe, "3D segmentation of thyroid ultrasound images using active contours," *Current Directions Biomed. Eng.*, vol. 2, no. 1, pp. 467–470, Jan. 2016.

[33] B. Klucinec, M. Scheidler, C. Denegar, E. Domholdt, and S. Burgess, "Transmissivity of coupling agents used to deliver ultrasound through indirect methods," *J. Orthopaedic Sports Phys. Therapy*, vol. 30, no. 5, pp. 263–269, May 2000.
[34] S. Gehlbach, "Frequency diversity speckle processing," *Ultrason. Imag.*, vol. 9, no. 2, pp. 92–105, Apr. 1987.
[35] C. Yoon, G.-D. Kim, Y. Yoo, T.-K. Song, and J. H. Chang, "Frequency equalized compounding for effective speckle reduction in medical ultrasound imaging," *Biomed. Signal Process. Control*, vol. 8, no. 6, pp. 876–887, Nov. 2013.
[36] Y. Yu and S. T. Acton, "Speckle reducing anisotropic diffusion," *IEEE Trans. Image Process.*, vol. 11, no. 11, pp. 1260–1270, Nov. 2002.
[37] T. F. Chan and L. A. Vese, "Active contours without edges," *IEEE Trans. Image Process.*, vol. 10, no. 2, pp. 266–277, Feb. 2001.
[38] T. J. Hall, M. Bilgen, M. F. Insana, and T. A. Krouskop, "Phantom materials for elastography," *IEEE Trans. Ultrason., Ferroelectr., Freq. Control*, vol. 44, no. 6, pp. 1355–1365, Nov. 1997.
[39] S. Namdari, R. P. Donegan, N. Dahiya, L. M. Galatz, K. Yamaguchi, and J. D. Keener, "Characteristics of small to medium-sized rotator cuff tears with and without disruption of the anterior supraspinatus tendon," *J. Shoulder Elbow Surgery*, vol. 23, no. 1, pp. 20–27, Jan. 2014.
[40] J. S. Ullom, M. L. Oelze, and J. R. Sanchez, "Speckle reduction for ultrasonic imaging using frequency compounding and despeckling filters along with coded excitation and pulse compression," *Adv. Acoust. Vib.*, vol. 2012, pp. 1–16, May 2012.

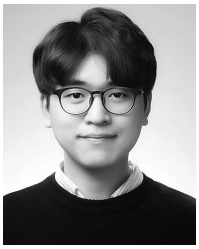

MOON HWAN LEE received the B.S. degree in electronic engineering from Kyungpook National University, Daegu, South Korea, in 2019. He is currently pursuing the integrated Ph.D. degree with the Department of Information and Communication Engineering, Daegu Gyeongbuk Institute of Science and Technology, Daegu.

His current research interests include ultrasound imaging and analysis systems.

JUN-YOUNG KIM received the M.D. and Ph.D. degrees in orthopedic surgery from Kyungpook National University, Daegu, South Korea, in 2014 and 2018, respectively.

He is currently an Assistant Professor with the Department of Orthopedic Surgery, Daegu Catholic University College of Medicine, Daegu. His research interests include arthroplasty and arthroscopy in shoulder and elbow joint.

KYUNGSU LEE received the B.S. degree in computer science from Handong Global University, Pohang, South Korea, in 2018. He is currently pursuing the integrated Ph.D. degree with the Department of Information and Communication Engineering, Daegu Gyeongbuk Institute of Science and Technology, Daegu, South Korea.

His research interest includes deep-learning in the biomedical application.

CHANG-HYUK CHOI received the M.D. and Ph.D. degrees from Kyungpook National University, Daegu, South Korea, in 1986 and 2004, respectively. He has provided orthopedic training at Kyungpook National University Hospital, from 1990 to 1994. He was a Fellow of the Prof. Lu Bigliani at the Shoulder Service of the Columbia Medical Center, from 1999 to 2000.

He has been the Faculty Member of the Department of Orthopedic Surgery, School of Medicine, Catholic University of Daegu, Daegu, where he is currently a Professor. He has published 110 articles in the peer-reviewed journals. His clinical and research interests include arthroscopic surgery in shoulder joint, arthroplasty in shoulder and elbow joint, and ultrasound for diagnosis and treatment in shoulder joint.

JAE YOUN HWANG (Member, IEEE) received the B.S. degree in electrical engineering from Korea University, Seoul, South Korea, in 2001, the M.S. degree in biomedical engineering from Seoul National University, Seoul, in 2003, and the Ph.D. degree in biomedical engineering from the University of Southern California, Los Angeles, CA, USA, in 2009.

He is with the faculty of the Department of Information and Communication Engineering, Daegu Gyeongbuk Institute of Science and Technology, Daegu, South Korea, where he is currently an Associate Professor. His current research interests include the development of a multimodality imaging systems based on high frequency ultrasound and optical techniques, and the development of novel mobile healthcare systems for the diagnosis of various diseases.